A wireless, skin-interfaced biosensor for cerebral hemodynamic monitoring in pediatric care

Alina Y. Rwei[a,b,1,2], Wei Lu[a,1], Changsheng Wu[a,1], Kelia Human[a], Emily Suen[a], Daniel Franklin[a,c], Monica Fabiani[d,e], Gabriele Gratton[d,e], Zhaoqian Xie[f], Yujun Deng[g], Sung Soo Kwak[a,h], Lizhu Li[i], Carol Gu[a], Alanna Liu[a], Casey M. Rand[j], Tracey M. Stewart[j], Yonggang Huang[a,c,k,l], Debra E. Weese-Mayer[j,m,2], and John A. Rogers[a,c,k,n,o,p,2]

[a]Querrey Simpson Institute for Bioelectronics, Northwestern University, Chicago, IL 60208; [b]Department of Chemical Engineering, Delft University of Technology, 2629 HZ Delft, The Netherlands; [c]Department of Materials Science and Engineering, Northwestern University, Evanston, IL 60208; [d]Beckman Institute, University of Illinois at Urbana–Champaign, Urbana, IL 61801; [e]Psychology Department, University of Illinois at Urbana-Champaign, Champaign, IL 61820; [f]State Key Laboratory of Structural Analysis for Industrial Equipment, Department of Engineering Mechanics, International Research Center for Computational Mechanics, Dalian University of Technology, 116024 Dalian, China; [g]State Key Laboratory of Mechanical System and Vibration, Shanghai Jiao Tong University, 200240 Shanghai, China; [h]School of Advanced Materials Science and Engineering, Sungkyunkwan University, 16419 Suwon, Republic of Korea; [i]Department of Electronic Engineering, Tsinghua University, 100084 Beijing, China; [j]Department of Pediatrics, Division of Autonomic Medicine, Center for Autonomic Medicine in Pediatrics, Stanley Manne Children's Research Institute, Ann & Robert H. Lurie Children's Hospital of Chicago, Chicago, IL 60611; [k]Department of Mechanical Engineering, Northwestern University, Evanston, IL 60208; [l]Department of Civil and Environmental Engineering, Northwestern University, Evanston, IL60208; [m]Department of Pediatrics, Pediatric Autonomic Medicine, Feinberg School of Medicine, Northwestern University, Chicago, IL 60611; [n]Department of Biomedical Engineering, Northwestern University, Evanston, IL 60208; [o]Department of Chemistry, Northwestern University, Evanston, IL 60208; and [p]Department of Neurological Surgery, Feinberg School of Medicine, Northwestern University, Chicago, IL 60208

Contributed by John A. Rogers, October 22, 2020 (sent for review September 21, 2020; reviewed by Ravinder Dahiya and Omer Inan)

The standard of clinical care in many pediatric and neonatal neurocritical care units involves continuous monitoring of cerebral hemodynamics using hard-wired devices that physically adhere to the skin and connect to base stations that commonly mount on an adjacent wall or stand. Risks of iatrogenic skin injuries associated with adhesives that bond such systems to the skin and entanglements of the patients and/or the healthcare professionals with the wires can impede clinical procedures and natural movements that are critical to the care, development, and recovery of pediatric patients. This paper presents a wireless, miniaturized, and mechanically soft, flexible device that supports measurements quantitatively comparable to existing clinical standards. The system features a multiphotodiode array and pair of light-emitting diodes for simultaneous monitoring of systemic and cerebral hemodynamics, with ability to measure cerebral oxygenation, heart rate, peripheral oxygenation, and potentially cerebral pulse pressure and vascular tone, through the utilization of multiwavelength reflectance-mode photoplethysmography and functional near-infrared spectroscopy. Monte Carlo optical simulations define the tissue-probing depths for source–detector distances and operating wavelengths of these systems using magnetic resonance images of the head of a representative pediatric patient to define the relevant geometries. Clinical studies on pediatric subjects with and without congenital central hypoventilation syndrome validate the feasibility for using this system in operating hospitals and define its advantages relative to established technologies. This platform has the potential to substantially enhance the quality of pediatric care across a wide range of conditions and use scenarios, not only in advanced hospital settings but also in clinics of lower- and middle-income countries.

wearable electronics | near-infrared spectroscopy | bioelectronics | cerebral hemodynamics

Over 900,000 children with ages between 0 and 19 y in the United States suffer from neurological injuries linked to irregular cerebral perfusion every year, with causes ranging from genetic mutations (1), premature birth (2), cardiac diseases (3), surgical intervention (4), and physical impacts (5). Such impaired cerebral perfusion may lead to brain damage (6), persistent neurologic disability (7), or death (6). These risks can be particularly high in certain pediatric populations (5). Specifically, premature infants with birth weights less than 1,500 g are prone to cerebral tissue injuries due to their fragile cerebral vasculature, underdeveloped autoregulation system (8), and the incomplete fusion of the skull plates (9); 25 to 35% of such infants develop periventricular–intraventricular hemorrhage due to significant fluctuations in arterial blood pressure or obstruction of the venous system, and up to 50% develop diffuse white matter injury due to disturbances in heart rate (HR) and cardiac output, inadequate blood supply to the white matter, and/or limited ability to autoregulate cerebral blood flow. Such cerebral perfusion complications are linked to persistent neurodevelopmental impairment and higher risks of death (2, 10). Pediatric subjects with congenital heart disease, traumatic brain injury, autoregulatory disorders, multiple organ dysfunction syndrome, or infections are under high risk of impaired cerebral autoregulation and long-term neurological damage (3, 5, 11–13). As a result, continuous monitoring of cerebral hemodynamics on pediatric subjects is now the standard of care in many pediatric and neonatal neurointensive care units and a subset of cardiac intensive

Significance

Continuous monitoring of cerebral hemodynamics is critical for safeguarding the healthy neurodevelopment of pediatric patients. This paper introduces a soft, flexible, miniaturized wireless system for real-time, continuous monitoring of systemic and cerebral hemodynamics for such purposes. Clinical studies on pediatric subjects with ages between 0.2 and 15 y and with various racial backgrounds validate opportunities for practical use in operating hospital environments. This platform may significantly enhance the quality of care of pediatric patients, particularly those at risk for cerebral and neurodevelopmental impairments in developed and developing world settings alike.

Author contributions: A.Y.R., D.E.W.-M., and J.A.R. designed research; A.Y.R., W.L., C.W., K.H., E.S., S.S.K., L.L., C.G., A.L., C.M.R., T.M.S., and D.E.W.-M. performed research; A.Y.R., W.L., D.F., Z.X., Y.D., and Y.H. contributed new reagents/analytic tools; A.Y.R., M.F., G.G., and J.A.R. analyzed data; and A.Y.R., W.L., D.F., Z.X., and J.A.R. wrote the paper.

Reviewers: R.D., University of Glasgow; and O.I., Georgia Institute of Technology.

The authors declare no competing interest.

[1]A.Y.R., W.L., and C.W. contributed equally to this work.

[2]To whom correspondence may be addressed. Email: a.y.rwei@tudelft.nl, DWeese-Mayer@luriechildrens.org, or jrogers@northwestern.edu.

This article contains supporting information online at https://www.pnas.org/lookup/suppl/doi:10.1073/pnas.2019786117/-/DCSupplemental.

First published November 30, 2020.

care units, with the aim of identifying risk and decreasing mortality, morbidity, and negative neurodevelopmental outcomes (14–16).

Current technologies for evaluating cerebral regional blood flow and oxygenation include transcranial ultrasound (17), magnetic resonance imaging (18), and cerebral near-infrared spectroscopy (NIRS) (19). The former two options have limited effectiveness due to their intermittent (as opposed to continuous) manner of use. Standard devices for cerebral NIRS rely on continuous monitoring from sensors physically attached onto the skin and tethered to separate base stations via hard wires, thereby limiting the subject's range of motion, impeding engagements with parents and healthcare workers, and imposing physical and economic barriers to widespread, routine use. Although recent reports describe wireless NIRS systems for adults (20, 21), their relatively large sizes, rigid designs, and heavy construction are nonideal for children, especially infants at high risk for iatrogenic skin injuries due to the fragility associated with their immature, delicate skin (22) and the high degree of curvature associated with their small heads. A technology that overcomes these limitations has great potential utility in pediatric and neonatal care.

This paper reports a soft, flexible, wireless cerebral hemodynamic monitoring device designed specifically for these infants and children. The key attributes include miniaturized dimensions, lightweight construction, gentle interfaces to the skin and shape conformability to the heads of even the smallest premature neonates. In addition to the advanced mechanics and physical form factors, these devices feature 1) multiphotodiode systems with four source–detector distances to allow simultaneous probing of systemic and cerebral hemodynamics and 2) replaceable, magnetically coupled batteries to minimize size and weight and to support options for replacement while the device remains adhering to the patient's skin. Monte Carlo modeling of the optics defines the probing depth through the skin and skull and into the brain, using geometries defined by MRI profiles of the head and cerebral tissue. Clinical studies on pediatric patients ranging from 0.2 to 15 y of age with and without impaired cerebral autoregulation validate the clinical applicability of this system.

Results

Design Layouts and Mechanical Characteristics. Fig. 1*A* presents an exploded schematic illustration of the technology. The miniaturized, mechanically compliant design allows gentle placement on the curved skin of a child's forehead via a medical-grade silicone adhesive, thereby enabling wireless, real-time monitoring of cerebral physiological signals, including cerebral oxygenation, cerebral vascular tone, pulse oxygenation, and HR. The overall layout includes a flexible printed circuit board with two main units: 1) a Bluetooth low-energy (BLE) system on a chip (SoC) module (nRF52832; Nordic Semiconductor) with associated components for power regulation and wireless communication and 2) an optical sensor for continuous monitoring of systemic and cerebral hemodynamics. The construction involves a process of folding the individual islands to reduce the overall size of the system, as shown in *SI Appendix*, Fig. S1. Encapsulation with a medical-grade silicone elastomer yields a compact device with dimensions of 33 × 16 × 3 mm and a mass of 2.8 g, approximately an order of magnitude lighter than NIRS probes currently used in the clinic. Data pass wirelessly from the sensor to a BLE-enabled device such as a tablet computer or a smartphone for real-time graphical display, data storage, and processing. Together, these features form the basis of a wireless cerebral hemodynamic sensor with applicability across a wide range of clinical settings and subjects, focused on, but not limited to, the pediatric population.

A modular, encapsulated battery electrically and mechanically couples to the device via embedded magnets (Fig. 1*B*), with a configuration of polarities that enforces proper orientation. This strategy 1) allows for replacement of the battery without disrupting the device–skin interface, thereby eliminating the risk of skin injury and disturbance of the optical coupling interface, and 2) mechanically decouples the rigid battery unit from the device for improved bendability and compliance onto highly curved anatomical features. Caregivers can select batteries with capacities to support operating lifetimes that meet requirements for a range of use cases: A CR1220 rechargeable coin cell battery with a capacity of 8 mAh allows for an operating time of 1 h, whereas a rechargeable lithium-polymer battery with a capacity of 18 mAh and 45 mAh can operate for 6 h and 14 h, respectively. Operational details such as the duty cycle and the power supplied to the light-emitting diodes (LEDs) can be refined to extend these times. The size and shape of the battery can be designed to avoid the risk of choking for children under age 3 y, as shown in our previous work (23).

The sensor unit features a pair of LEDs that emit at wavelengths of 740 nm and 850 nm along with an array of silicon photodiodes to define source–detector distances of 5, 10, 15, and 20 mm. This layout allows recordings of hemodynamic signals at different tissue depths for detection of peripheral and cerebral hemodynamics. The optical sensor includes a soft encapsulating layer on the bottom, skin-facing side of the system based on a black silicone material that serves as an optical barrier to eliminate effects of parasitic optical responses to the ambient environment and to light that passes directly from the LEDs without transmission through the tissues (Fig. 1*C*). The device employs a thin, 100-μm-thick layer of transparent polydimethylsiloxane (PDMS) patterned and aligned to form soft optical windows between the skin and the LEDs and photodetectors. This layer also reduces the change in refractive index at the skin interface, to decrease the reflectance relative to that expected for polymer–air or air–tissue interfaces. Specifically, given the refractive index of the LED silicone encapsulant, the scalp and the PDMS ($n_{\mathrm{LED\ Encap}} \approx 1.45, n_{scalp} \approx 1.37, n_{\mathrm{PDMS}} \approx 1.43$), these PDMS windows improve the coupling efficiency of light into the tissue by ~6% based on a simple estimation using Fresnel reflection at normal incidence ($T_{\mathrm{LED\ Encap}\rightarrow\mathrm{air}\rightarrow\mathrm{scalp}} = 0.9427, T_{\mathrm{LED\ Encap}\rightarrow\mathrm{PDMS}\rightarrow\mathrm{scalp}} = 0.9995$). This same improvement occurs as light returns at near-normal incidences from the tissue into the photodiodes, but with additional benefits in reducing total internal reflection (TIR) for collection of light that arrives at angles above the cutoff ($TIR_{scalp\rightarrow air} = 46.8°, TIR_{scalp\rightarrow PDMS} = NA$). This same soft interface also improves mechanical coupling to the skin. The device naturally adheres to the contours of the skull and provides a stable base for optical measurements in a manner that eliminates parasitic effects of relative motions of the device to the surface of the skin. Also, without the PDMS, the air gap between the optical elements and scalp could allow the distance and orientation of the LED/photodiodes to vary with respect to the scalp, thereby introducing additional sources of error, variability, and artifacts.

A key feature of this platform, especially for its potential deployment into lower- and middle-income countries, is its use of standard, cost-effective, off-the-shelf electrical components and conventional manufacturing schemes. Within these constraints, advanced concepts in hybrid flexible electronics can nevertheless yield soft and conformable properties at the system level, to allow mounting on the highly curved anatomical features and fragile skin of the youngest neonates. Specifically, guided by three-dimensional (3D) finite element analysis (FEA) of the mechanics, serpentine interconnects with optimized geometries connect a collection of islands that support components for 1) power regulation, 2), BLE SoC, and 3) bidirectional radio communication. The result is a bendable (Fig. 1*D*) and twistable (Fig. 1*E*) platform that allows for a gentle skin interface and a nonirritating but robust optical and mechanical coupling to the skin. The FEA results in Fig. 1*F* indicate that the maximum equivalent strains in the Cu traces are below 0.3% (the limit for

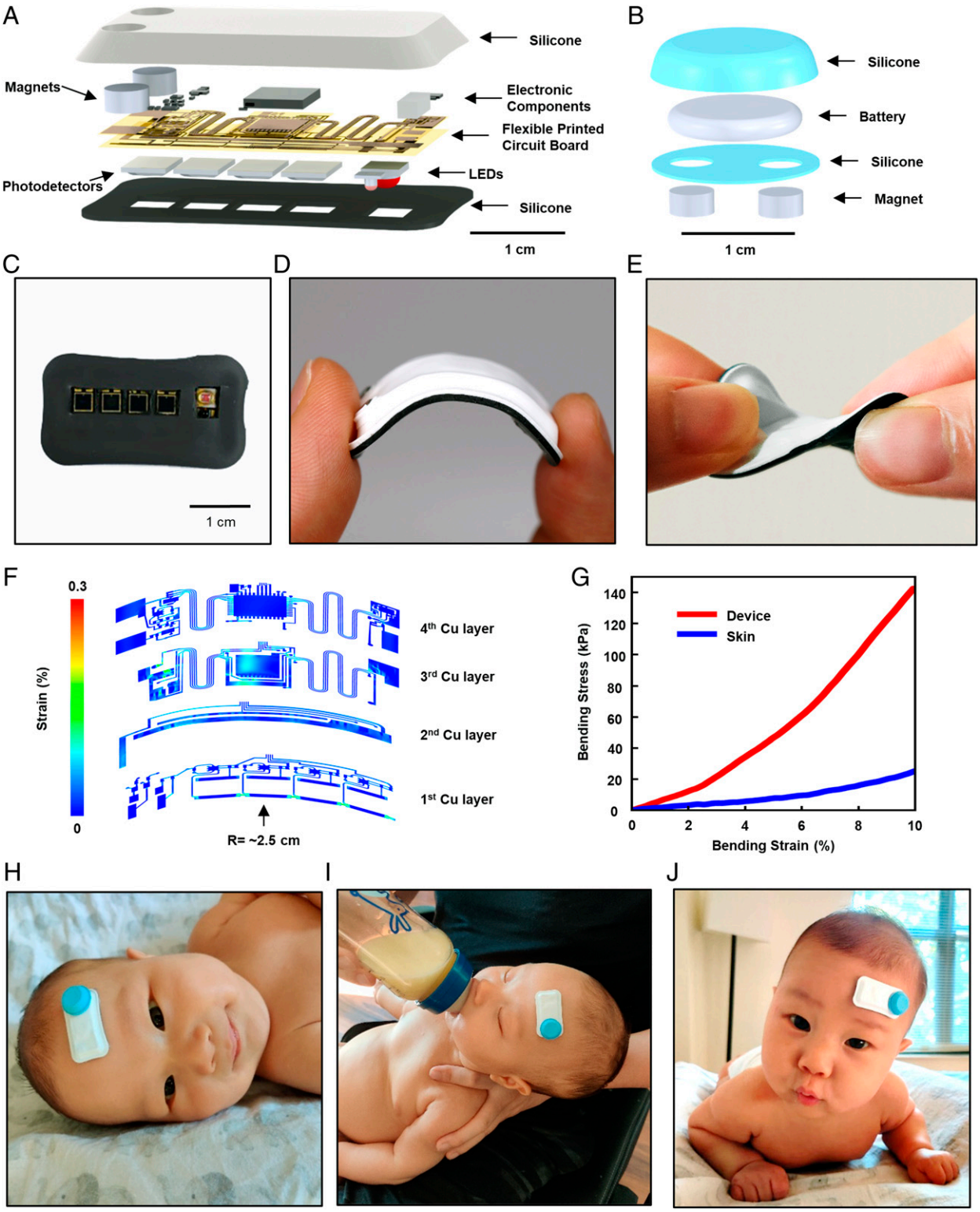

Fig. 1. Design and mechanical characterization of a soft, wireless device for cerebral hemodynamic monitoring on pediatric subjects. (*A* and *B*) Schematic illustration and exploded view of (*A*) a device with (*B*) a modular, rechargeable coin cell battery. The main body consists of serpentine interconnects between islands of electrical components for wireless operation and optical tissue profiling, with four photodiodes each featuring a distinct source–detector distance. The main body and the modular battery both feature a pair of magnets for mechanical and electrical coupling, all encapsulated within soft, medical-grade silicone. (*C*) Photograph of the skin-oriented side of the main device unit, with a pair of LEDs and four photodetectors encapsulated between a black silicone optical barrier and coated with transparent PDMS for effective optical coupling. (*D* and *E*) Photograph of a device upon mechanical stresses of (*D*) bending and (*E*) twisting. (*F*) Computed strain distribution in the copper layers (first Cu layer is the closest to skin) of the device with a bending radius of 2.5 cm. (*G*) Mechanical characterization of the device main unit compared with pig skin using a three-point flexural test. (*H*–*J*) Photographs of a device with a modular battery mounted on the forehead of a 9-wk-old infant during (*H*) resting, (*I*) feeding, and (*J*) tummy time.

plastic deformation) for a bending radius of 2.5 cm, which is much smaller than that required for a neonatal forehead [the head of a 24-wk gestational age neonate has a radius of ∼3.5 cm (24)]. Fig. 1 *D*–*G* shows the device bent to a radius of 3.5 cm and twisted by >30°. A three-point flexural test (Fig. 1*G*) indicates a flexural modulus of 780 ± 70 kPa (mean ± SD), comparable to that of porcine skin at the same thickness (120 ± 20 kPa; mean ± SD). *SI Appendix*, Table S1 presents the cost structure associated with all aspects of the device, including components, encapsulation materials, and fabrication. The analysis reveals a cost of under $25 per device. These results highlight a robust yet flexible design strategy with cost, manufacturability, and an ability to accommodate realistic physiological motions with little constraint on the underlying skin as key considerations.

Fig. 1 *H*–*J* show the device interfaced with a 9-wk-old infant during daily activities such as resting, feeding, and tummy time. Here, a coin cell modular battery (CR1220) serves as the power supply. The miniaturized design enables flexible placement on the limited anatomical area of the infant's forehead, and the low modulus construction minimizes stresses and irritation at the skin interface. The wireless operation eliminates the complications of wires associated with conventional medical devices, thereby allowing the closely supervised infant to behave naturally and without constraint, to facilitate movement, growth, and development, while continuously monitoring key physiological parameters.

These devices, when placed on different regions of the head, can monitor changes in optical parameters (e.g., light absorption and scattering) of the brain using functional NIRS (fNIRS). fNIRS uses a diffuse optical imaging approach to provide measures of the concentration of oxy- and deoxyhemoglobin, as well as tissue oxygenation level, in particular brain regions. fNIRS provides, therefore, data of significance for cognitive neuroscience due to their noninvasive, portable, and continuous monitoring capabilities (25). For example, studies show that placement of an NIRS probe on the neonatal temporal area can detect changes in regional blood flow indexing cortical activation correlated with auditory stimulation (26). Current fNIRS devices rely on wired systems; although portable systems have been developed, they are bulky in size with the need for separate backpacks for the electronic components (25). The soft mechanical properties and small sizes of the devices presented here enable placement and simultaneous operation at multiple locations on an infant's head, constrained only by the confounding effects of high-density hair-bearing regions. *SI Appendix*, Fig. S2 demonstrates the placement of two devices on an infant: one on the anterior fontanelle and one above the temporal lobe, reflecting the potential to measure cerebral signals from multiple locations. The BLE interface supports operation of 20 devices simultaneously, without reductions in sampling rate. The device is reusable after the replacement of the skin-interfacing adhesive and disinfection of the device with alcohol wipes, as according to guidelines from the Centers for Diseases Control and Prevention (27).

Optical Modeling. Optical simulations based on Monte Carlo analysis and realistic magnetic resonance images of the skin, skull, and brain tissues of pediatric patients elucidate the physiological basis of the measurements, guide the choices of source–detector distances and their corresponding probe tissue depths, and estimate the propagation of light within the cerebral tissues for placement on the forehead. The specific implementation of the simulations reported here allows for direct use of physiologically realistic, tetrahedral meshes created from medical images (28, 29). Fig. 2 *A* and *B* shows MRI data from a representative term-born infant [Neonatal Brain Atlas (30)]. Manually segmenting the volumetric MRI data into tissue regions (scalp, skull, cerebral spinal fluid, gray matter, and white matter) provides the labeled overlays of Fig. 2 *A* and *B* and allows discretization into tetrahedral meshes with dynamic sizing (minimum 0.1 mm, maximum 1.5 mm) [NIRFAST-Slicer (31, 32)]. Optical properties of the respective materials evaluated for the specific wavelengths used here (740 nm and 850 nm; *SI Appendix*, Table S2) map to the mesh.

The Monte Carlo approach statistically builds models of the light propagation through a volume by tracking the trajectories of millions/billions of photons as they undergo scattering and absorption events. Fig. 2*C* shows the resulting normalized fluence through the simulation volume for a given source location and input direction (red dot). Black dashed lines indicate tissue boundaries; white dashed lines represent light fluence contour lines in 1 $\log_{10}$ increments. Photons that reach the photodiodes (indicated by green dots, 7.5 mm^2) represent back-scattered light available for detection. Tracking the pathlengths of these detected photons serves as a mechanism to deduce the fraction of detected light that penetrates to a given material layer. The results in Fig. 2*D* show the relative partial pathlengths at each detector as a function of propagation within each respective tissue type. As expected, the percentage of light that propagates through shallow tissues (e.g., scalp and bone tissue) increases with decreasing source–detector separation. At separations of 15 mm and 20 mm, a significant percentage of light propagates through neural tissue. These relative pathlengths correlate to the amount of static signal (direct current, DC) vs. hemodynamically modulated signal (alternating current, AC) measured by the device, thereby allowing measurements of changes in oxygenation from the respective tissue layers. In this manner, the array of detectors allows simultaneous depth-resolved oximetry and supports advanced schemes in reducing the effects of motion artifacts by eliminating common noise. The selection of source–detector distances of this platform follow explicitly from considerations of small head geometries and realistic tissue thicknesses of pediatric patients, optimized for infants. Guided by optical simulation results, a choice of source–detector distances of 15 mm and 20 mm supports probing of pediatric cerebral hemodynamics, with distances of 5 mm and 10 mm for probing of peripheral tissues.

Optical and Electrical Characteristics. This system utilizes a pair of LEDs at different NIR wavelengths to optimize transmission for measurement of deep tissue cerebral hemodynamics. Tissue chromophores such as hemoglobin and melanin have strong absorption at wavelengths <650 nm and water absorbs at wavelengths >900 nm, yielding an optimal window for transmission between wavelengths of 650 nm and 900 nm (33). Because of the different absorption spectra of oxy- and deoxyhemoglobin, concurrent measurements at multiple wavelengths (appropriately chosen to be relatively more sensitive to one or the other chromophores) can be used to independently estimate the concentration of these chromophores (provided that the optical pathlength in tissue for each wavelength can be estimated), as well as their sum (total hemoglobin concentration). As the optical absorbance spectrum of hemoglobin undergoes distinct changes based on its oxygenation state (Hb and HbO_2), optical profiling with two or more wavelengths serves as the basis for determining tissue oxygenation (34). Wavelengths of 740 nm and 850 nm for cerebral hemodynamic detection (*SI Appendix*, Fig. S3*A*) satisfy two criteria to maximize the sensitivity because they lie 1) above and below the isosbestic point of Hb and HbO_2 (∼805 nm) (35) and 2) within the NIR window of 700 and 900 nm.

A compact circuit design (29 × 1.2 × 0.4 mm) drives these LEDs in a low-duty-cycle mode, alternatively (*SI Appendix*, Fig. S3*B*), processes and sample signals from all four photodiodes, filters and packages the raw data, and wirelessly communicates to an external device via Bluetooth protocols, as shown in Fig. 3*A*. The 740-nm (QBHP684-IR4XU; QT-Brightek Co.) and 850-nm LEDs (SFH 4059; OSRAM Opto Semiconductor Inc.) receive power from the driving circuit, modulated by the microcontroller. For present purposes, the currents for the 740- and 850-nm LEDs

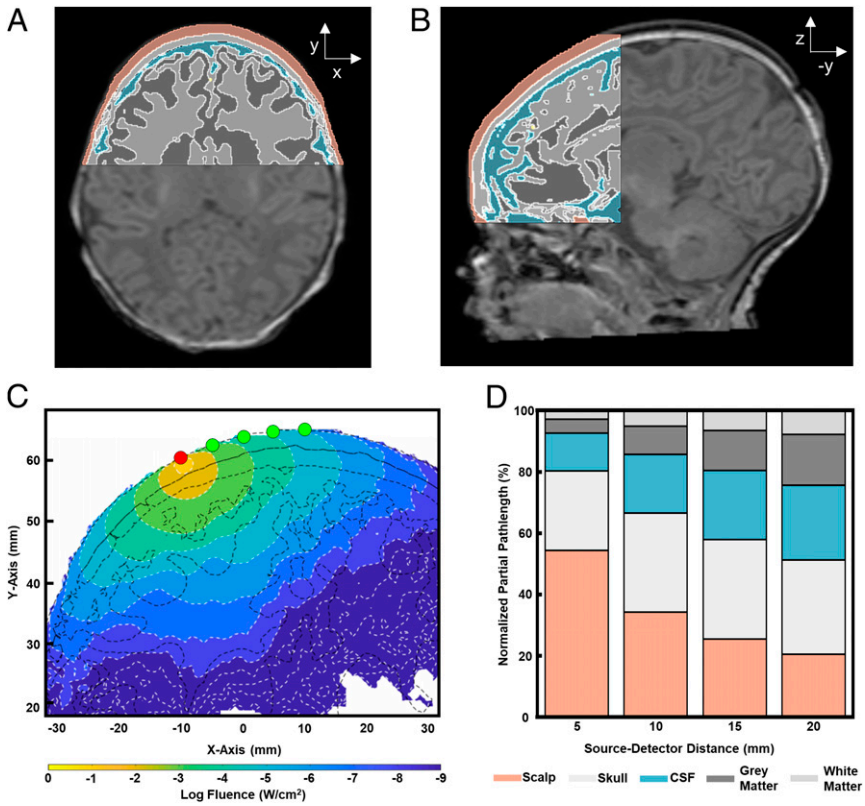

Fig. 2. Optical distribution of NIR light in the cerebral tissue. (*A* and *B*) Representative MRI data from a term-born infant and manually defined scalp (coral), skull (light gray), cerebral spinal fluid (blue), gray matter (dark gray), and white matter (gray) in the (*A*) axial view and (*B*) sagittal view. (*C*) Computed optical distribution of NIR light (850 nm) via Monte Carlo simulation (red: light source; green: photodetectors). (*D*) Relative partial pathlength of light at each source–detector distance within each respective tissue type.

are 10.0 mA and 11.7 mA, yielding irradiance values of 11.0 and 4.8 mW, respectively (*SI Appendix*, Fig. S3 *A* and *B*). A duty cycle, defined as the ratio between the LED pulse duration and the duration of the cycle, of 10% (*SI Appendix*, Fig. S3*B*) balances signal quality with power consumption and temperature control. Upon operating for 1 h continuously on human skin, the skin temperature does not change in a physiologically relevant fashion (i.e., remains below 37 °C; *SI Appendix*, Fig. S4). Four photodetectors (PDs) are evenly distributed along the middle line of the two LEDs, with an edge-to-edge spacing of 5 mm. Each photodetector has a radiant sensitive area of 7.5 mm^2 and a quantum efficiency of 70% for 850 nm and 59% for 740 nm. The output of each PD passes through a transimpedance amplifier to convert the photocurrent to an amplified voltage signal. A linear relationship connects these voltages to the detected irradiance (*SI Appendix*, Fig. S3*C*). The slope of this relationship depends on electronic amplification factors chosen based on the source–detector distance. Specifically, the amplification settings increase with distance to compensate for corresponding reductions in detected light. Four 14-bit analog–digital converters in parallel support signal sampling at a rate of 200 Sa/s, corresponding to 100 Sa/s for each LED channel from each PD. The signal-to-noise ratios of each PD are 59.0, 56.7, 58.4, and 54.5 dB, respectively, in the order of increasing source–detector distance when placed on the forehead of an African American female young adult. The microcontroller unit performs smoothing on the raw data with a finite impulse response 7-point moving average filter, providing a low-pass filter with cutoff frequency of 6.4 Hz. Data transfer occurs wirelessly to a personal computer through BLE protocols. A custom graphical user interface (GUI) software (*SI Appendix*, Fig. S3*B*) serves as a control interface and mechanism for data storage and display. Data are stored in the format of .txt files, for easy integration into standard data analysis packages.

Data Analytics and Validation. Continuous monitoring of cerebral hemodynamics is critical for the evaluation and detection of impaired cerebral autoregulation and its associated risk of brain injury during pediatric development, including infants with immature cerebral autoregulation systems (36), pediatric subjects with genetically induced autoregulation disorders such as congenital central hypoventilation syndrome (1) (CCHS), and during surgical procedures of the cardiac and respiratory systems (37). Cerebral oxygenation and vascular tone are two important indicators of cerebral hemodynamics. The former quantifies the amount of oxygenated hemoglobin in the cerebral tissue to evaluate tissue perfusion and the neuronal microenvironment, while the latter reflects the autoregulation response of the cerebral vascular system upon time-dependent differences in blood oxygenation concentration (38, 39). In addition to regional hemodynamics of the cerebral tissue, systemic hemodynamic parameters such as HR and arterial blood oxygenation provide further insights in the general health status of the subject, as part of the current standard of care (40). As time-dependent differences in regional hemodynamics are often associated with systemic hemodynamics, the integration of regional and systemic hemodynamics enables a wholistic evaluation of the subject's physiological state, which is especially critical for neonatal and pediatric subjects (41).

Fig. 3*C* outlines the procedures for extracting the cerebral oxygenation, pulse oxygenation, HR, and cerebral vascular tone from the measured data. Signals captured by PD1 and PD2, corresponding to source–detector distances of 5 mm and 10 mm, respectively, reflect

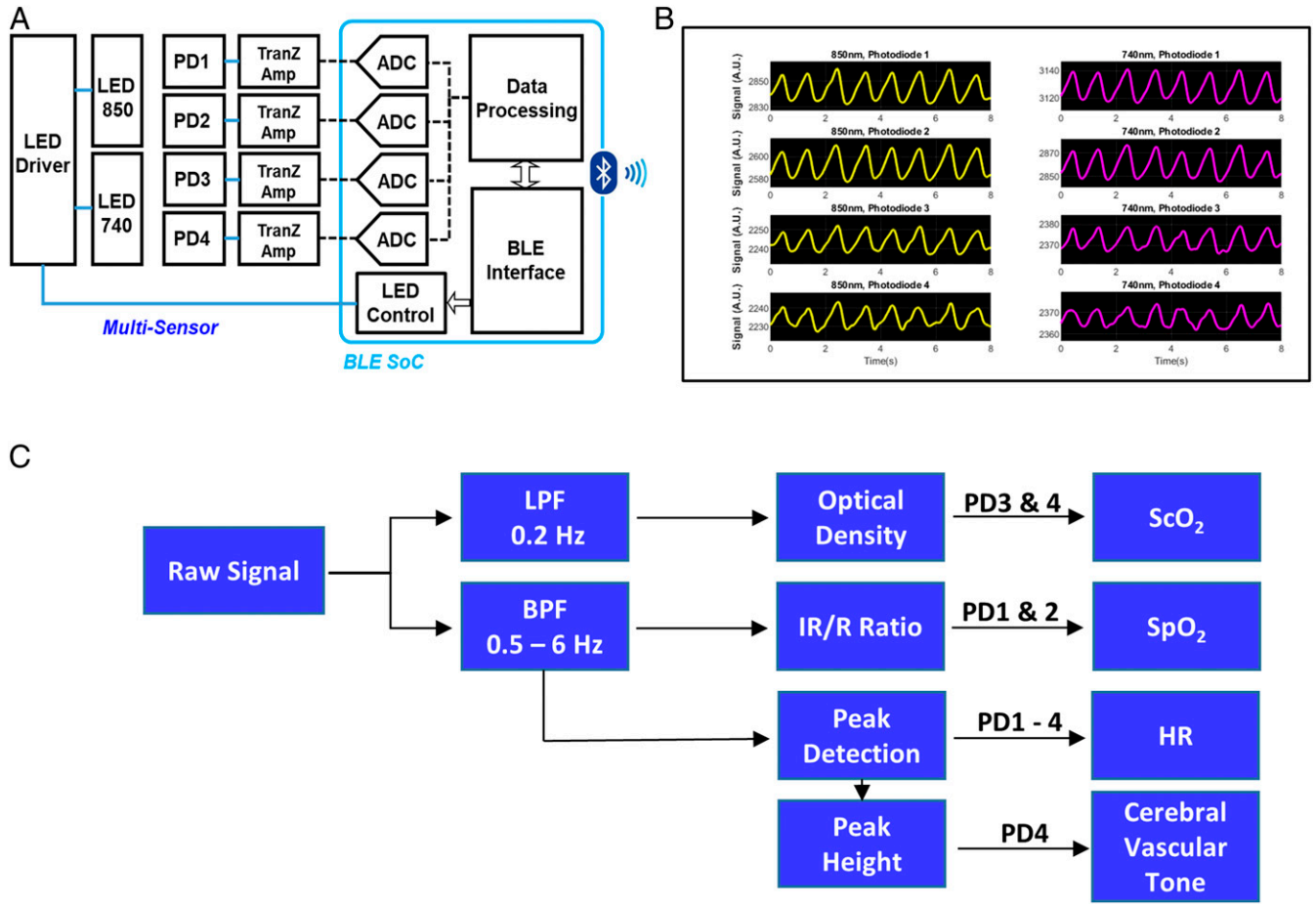

Fig. 3. Operational characteristics of our device for cerebral hemodynamics monitoring. (*A*) Schematic block diagram for our BLE electronic module. The module contains the LEDs and the driving circuit, PDs, and transimpedance amplifier circuits, a BLE microcontroller with a custom-developed program, and peripheral circuits. (*B*) GUI for the cerebral oximeter. The GUI supports real-time visualization, storage, and analysis of measurement data and provides a control interface for setting parameters for the BLE module. (*C*) Flowchart of the data analysis procedure for extraction of cerebral oxygenation (ScO_2), peripheral oxygenation (SpO_2), HR, and cerebral vascular tone. LPF = low-pass filter, BPF= band-pass filter, R = red, and IR = infrared. PD1, PD2, PD3, and PD4 correspond to source–detector distances of 5, 10, 15, and 20 mm respectively.

hemodynamics of shallow peripheral tissues to define arterial blood oxygenation levels (SpO_2); signals captured by PD3 and PD4, corresponding to distances of 15 mm and 20 mm, respectively, reflect hemodynamics of deep cerebral tissues to define the cerebral tissue oxygenation levels (ScO_2). Data from PD4 can be used to determine the cerebral vascular tone. All PDs contribute to the detection of HR.

Cerebral oxygenation corresponds to the nonpulsatile (DC) component of the blood volume (42). For analysis, the raw data from PD3 and PD4 first passes through a second-order Butterworth low-pass filter with a cutoff frequency of 0.2 Hz to extract the DC component. *SI Appendix*, Fig. S5 compares the oxygenation measurements determined with this platform to that from a standard, commercialized oxygenation probe (Swan–Ganz catheter; Edwards Lifesciences Corporation) in a controlled laboratory setting using commercially available fresh horse blood (Quad Five Inc.). The absorbance spectra of the oxygenated and deoxygenated blood show an expected decrease in absorbance of deoxygenated hemoglobin and increase in absorbance of oxygenated hemoglobin with wavelengths between 700 nm and 900 nm (*SI Appendix*, Fig. S5*A*). The measurements reflect these changes, in which the absorbance at 740 nm decreases and the absorbance at 850 nm increases upon oxygenation (*SI Appendix*, Fig. S5*B*). Oxygenation measurements calculated in this manner show a linear correlation with those obtained using the commercialized platform ($R^2 = 0.999$; *SI Appendix*, Fig. S5*C*).

Fig. 4*A* presents time-dependent variations of ScO_2 obtained from a healthy adult, in which the cerebral oxygenation decreases upon holding of the breath, defined as "full breath in and holding at end inspiration" (end inspiratory breath hold). Analysis using the Bland–Altman method shows a mean difference of 0.01 ± 0.9% (mean ± SD, $n = 3$; Fig. 4*B*) when compared to a medical-grade NIRS (INVOS 5100C Cerebral/Somatic Oximeter; Medtronic).

The pulsatile (AC) components of the data (presumed to reflect volumetric changes of arteries during each pulsation) can be obtained via a second-order Butterworth band-pass filter between 0.5 and 6 Hz and then used to calculate the SpO_2 (43). Fig. 4*C* presents time-dependent variations of SpO_2 obtained from a healthy adult, showing a decrease in arterial oxygenation upon holding of the breath. Analysis using the Bland–Altman method shows a mean difference of 0.35 ± 0.63% (mean ± SD, $n = 3$; Fig. 4*D*) when compared to a medical-grade finger SpO_2 probe (GE Dash 3000; GE Healthcare).

HR follows from peak detection of the AC component. Fig. 4*E* presents time-dependent variations of HR on a healthy adult, compared to measurements from a medical-grade finger probe (GE Dash 3000; GE Healthcare). Bland–Altman analysis shows a mean difference of −0.2 ± 1.51 bpm (mean ± SD, $n = 3$; Fig. 4*F*).

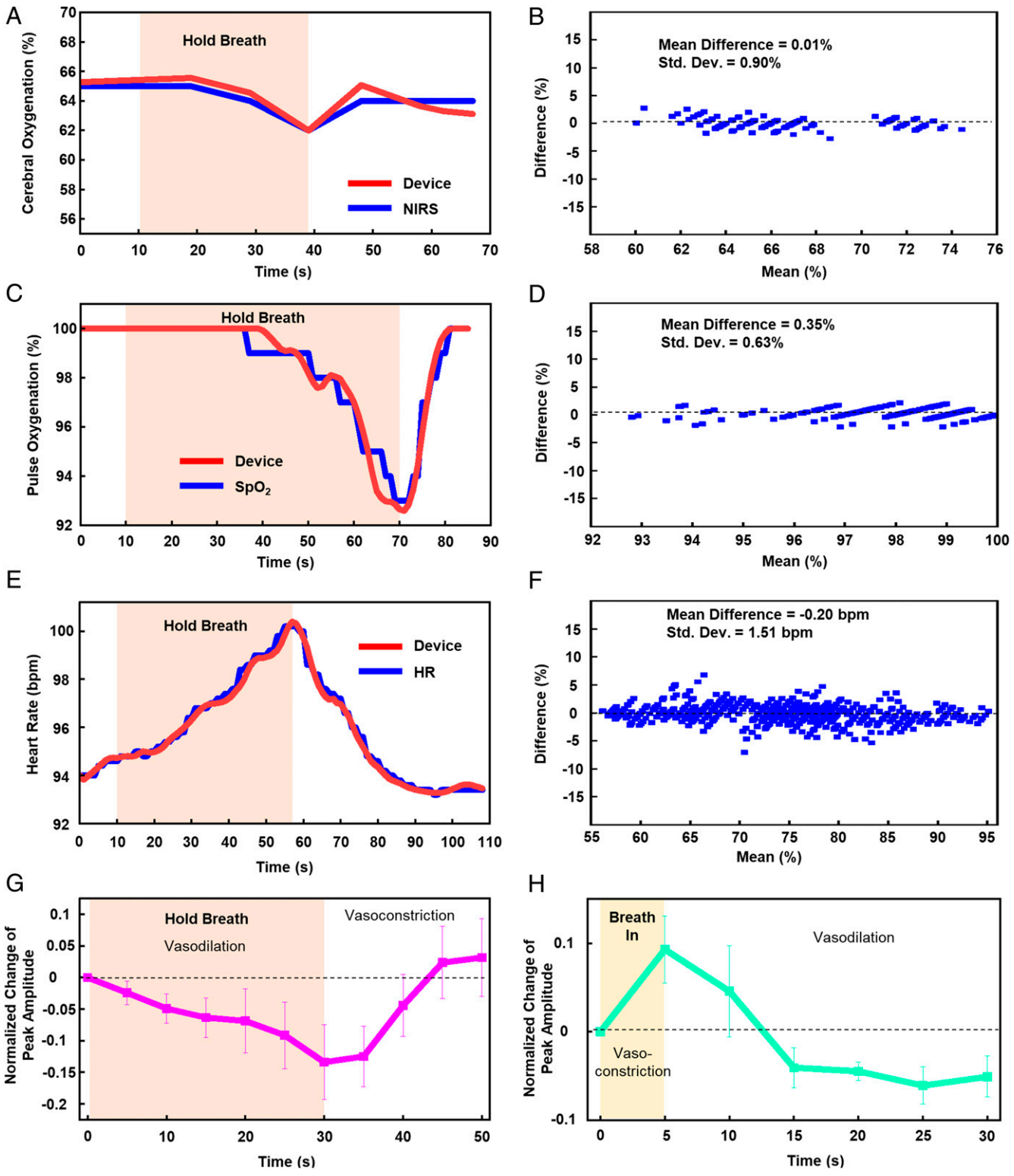

Fig. 4. Data collection of systemic and cerebral hemodynamics from healthy young adults. (*A*) Representative cerebral oxygenation measurements from our device and a commercialized NIRS instrument during end inspiratory breath-hold studies on a 20-y-old African American subject. (*B*) Bland–Altman analysis of cerebral oxygenation measurements between our device and a commercialized NIRS instrument ($n = 3$ subjects, three breath-hold events per subject). (*C*) Representative pulse oxygenation measurements from our device and a standard SpO_2 finger probe during end inspiratory breath-hold studies on a 29-y-old subject. (*D*) Bland–Altman analysis of pulse oxygenation measurements between our device and a commercialized SpO_2 finger probe ($n = 3$ subjects, three breath-hold events per subject). (*E*) Representative HR analysis from our device and a clinically used finger probe during end inspiratory breath-hold on a 19-y-old subject. (*F*) Bland–Altman analysis of HR analyses between our device and a medical-grade finger probe during end inspiratory breath-hold exercises ($n = 3$ subjects, three breath-hold events per subject). (*G* and *H*) Representative vascular tone and pulse pressure measurements from our device, reflected from the change of peak amplitude, during (*G*) end inspiratory breath-hold (eight events) and (*H*) breath-in (defined as deep inspiration, followed by immediate expiration, five events) exercises on a 16-y-old subject.

Recent advances in optical monitoring of cerebral activity suggest that cerebral vascular tone may correspond to peak-to-peak variations of the amplitude of individual arterial pulses, which, when assuming arterial compliance to be constant over the period of measurement, reflects the difference between systolic and diastolic arterial blood pressure, referred to as pulse pressure (44, 45). Pulse pressure decreases with vasodilation and increases with vasoconstriction. Fig. 4 *G* and *H* and *SI Appendix*, Fig. S6 present time-dependent variations of pulse pressure during breath-hold and deep breathe-in exercises by healthy adolescents and young adults ($n = 3$, ages 16, 19, and 20 y). During breath-hold, the pulse amplitude significantly decreases when compared with an initial 30-s baseline period ($P < 0.01$, eight breath-hold events per adult), indicating vasodilation and a corresponding decrease in pulse pressure (Fig. 4*G* and *SI Appendix*, Fig. S6, *Left*); during deep breathe-in exercises, the pulse amplitude significantly increases when compared to baseline ($P < 0.05$, five breathe-in exercises per adult), indicating vasoconstriction and a corresponding increase in pulse pressure (Fig.4*H* and *SI Appendix*, Fig. S6, *Right*). These advances suggest possibilities in convenient, routine, and noninvasive monitoring of dynamic cerebral autoregulation and cerebrovascular health without restraint on subject activity across all patient populations (46).

Pediatric Clinical Pilot Studies. Fig. 5 presents wirelessly captured cerebral oxygenation signals from eight pediatric subjects with *PHOX2B* mutation-confirmed CCHS and from four subjects with dizziness (without other health abnormalities). Age of these subjects range between 2 mo and 15 y, covering a range of skin colors and their corresponding optical absorption properties (*SI Appendix*, Table S3). Clinical assessments of the physiological function of the autonomic nervous system and respiratory control follow from four challenges: head-up tilt (HUT), hyperoxia, hypoxia, and hypoxia–hypercapnia. Hyperoxia primarily suppresses peripheral chemoreceptors, hypoxia primarily stimulates peripheral chemoreceptors, and hypoxia–hypercapnia stimulates both central and peripheral chemoreceptors (1). Fig. 5*A* shows the cerebral oxygenation response during the orthostatic challenge of HUT from an 8-y-old African American boy with CCHS. The results indicate a significant decrease in cerebral oxygenation upon tilting to a 70° upright position when compared with the initial 0° baseline period (Fig. 5*B*; $P < 0.01$, $n = 10$). Measurements using a wired, commercialized NIRS device (INVOS 5100C Cerebral/Somatic Oximeter; Medtronic), positioned on the opposite side of the forehead, confirm these findings. The HUT response is comparable to reported findings, in which a tilt-induced decrease in cerebral blood flow results in decrease of cerebral oxygenation.*

Fig. 5*C* presents results from a hyperoxia challenge on a 4-y-old Caucasian girl with CCHS. The protocol involves a 3-min clinical hyperoxia challenge following a baseline period of the same duration, per a published protocol (1). Cerebral oxygenation measured by the wireless platform indicates an increase during the hyperoxia challenge, confirmed by results from the commercial NIRS system. *SI Appendix*, Fig. S8 presents our results from a hypoxia–hypercapnia challenge on the same subject, with the same baseline protocol and a gas challenge of 14% O_2 and 7% CO_2 balanced with nitrogen (N_2). The wireless results show an initial decrease in cerebral oxygenation upon the initiation of the hypoxia-hypercapnia challenge, followed by an increase in cerebral oxygenation after 2 minutes of exposure and maintained during the recovery phase, confirmed by the commercial NIRS system. Fig. 5*D* presents results from a 13-y-old Hispanic girl with CCHS during a clinical hypoxia challenge with five breaths of nitrogen after a 3-min baseline period. Wirelessly obtained results show a decrease in cerebral oxygenation during the challenge, verified by the commercial system. These results are similar to those of previous reports (1).

Fig. 5*E* and *SI Appendix*, Fig. S7 presents a proof-of-concept demonstration of cerebral oxygenation monitoring on a 2-mo-old newborn engaged in normal daily age-appropriate activities. The results show a steady cerebral oxygenation trend. The wireless measurements, including autoregulatory challenges of subjects between age 4 and 15 y, and normal activity for subjects between age 0.2 and 2 y old, compare well with those of the commercial NIRS device, as analyzed by the Bland–Altman method (Fig. 5*F*). Results showed a mean difference of $-0.06 \pm 2.30\%$, demonstrating high accuracy and precision in operation for these testing conditions. The soft mechanics of the device allow for its removal from the skin in a two-step process, beginning with the disruption of the adhesion force at the edge of the device, followed by a slow, gentle removal of the thin adhesive layer from the skin. This sequence minimizes the potential for skin injury. Visual inspection confirmed the absence of skin effects related to wireless probe use.

Discussion

This paper introduces a class of soft, skin-interfaced, wireless devices for continuous monitoring of cerebral hemodynamics, with an emphasis for use on the most vulnerable pediatric and neonatal patients. The compliant, flexible device mechanics and the gentle skin contact serve as the basis for a skin-safe, conformable interface to the high curvature surfaces of the foreheads of infants across a wide range of ages (Fig. 1), including the youngest premature babies. The optical and mechanical aspects of the interface materials allow efficient optical coupling and robust bonding, for high signal quality and low motion artifacts. The miniaturized sizes of these devices allow placement on nearly any location across the small heads of pediatric subjects, limited only by dense, hair-bearing regions. Pilot studies in operating hospital environments indicate no negative skin effects during device operation. The skin-interfacing adhesives and the device encapsulation materials are similar to those tested on over 100 neonatal and pediatric subjects, including premature babies born as young as 24-wk gestational age, for up to 24 h at 8 wk of postnatal life without any negative skin effects on their fragile premature skin (23). These results further support the clinical safety and feasibility of the systems reported here.

The required operational lifetimes depend on the details of the clinical use case, according to which the engineering parameters, most notedly the duty cycle of LED irradiation and the sampling rate, can be optimized. A balancing consideration is that the signal-to-noise ratio generally decreases with the duty cycle (47). The results described previously utilize a 10% duty cycle, but studies of other related platforms suggest that a 5% duty cycle can support reliable operation, with an enhancement in battery life of ∼1.5 times (47). Sampling rate is determined based on the clinical requirements. The sampling frequency used here, 100 Hz, allows for high-resolution determination of SpO_2, HR, and cerebral vascular tone. Under an alternative-use case that requires only cerebral oxygenation, frequencies as low as a hundredth of a hertz can be considered, as described in commercialized systems (48), such that the power consumption would be decreased by ∼3.5 times, enhancing the operational lifetime of a given battery.

The Monte Carlo optical simulations quantify the underlying physics using realistic models, thereby serving as the basis for optimized selection of operating parameters for the LEDs and distances between the sources and detectors for the pediatric population. The differences in head size and tissue profiles of pediatric subjects, especially young infants, compared with adults are critically important considerations in this optimization. The

*C. Coleman et al., Pediatric Academic Societies Annual Research Conference, April 25–28, 2015, San Diego, CA.

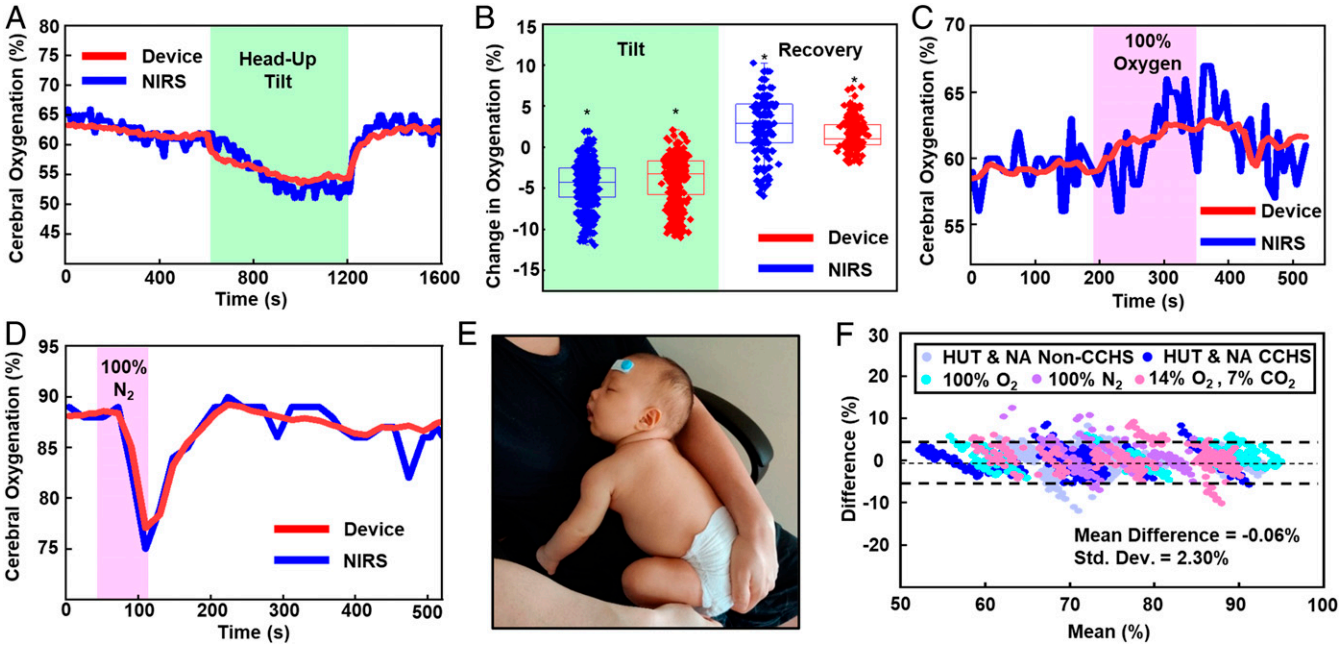

Fig. 5. Data collection from pediatric subjects with and without CCHS. (*A*) Representative NIRS measurements from our device and medical-grade NIRS on pediatric subjects during a HUT challenge on an 8-y-old African American boy with CCHS. (*B*) Relative changes in cerebral oxygenation of pediatric subjects measured by our device and a commercialized NIRS system during tilt phase and recovery phase relative to a 10-min baseline period ($n = 10$). Statistical analysis was performed by a paired Student t test. $^*P < 0.01$ when compared with baseline. A P value <0.05 was considered statistically significant. (*C*) Representative NIRS measurements during a hyperoxia challenge with 100% oxygen on a 4-y-old Caucasian girl with CCHS. (*D*) Representative NIRS measurements during a hypoxia challenge with 5 breaths of 100% nitrogen gas on a 13-y-old Hispanic girl with CCHS. (*E*) Photograph of our device on the 2-mo-old infant upon cerebral oxygenation measurements during normal activity. (*F*) Bland–Altman analysis of our device compared with a medical-grade NIRS device from HUT, hyperoxia (100% O_2), hypoxia challenges (100% N_2), and hypoxic–hypercapnia (14% O_2 and 7% CO_2 balanced with nitrogen [N_2]) with pediatric subjects aged 4 to 15 y and during normal activity (NA) with pediatric subjects aged 0.2 to 2 y.

computational framework reported here simulates the photon propagation pathway based on realistic tissue geometries, taking advantage of 3D medical imaging databases collected in hospitals from patients. Similar strategies can be used to define engineering parameters for detection of cerebral hemodynamics of age groups beyond those that represent the focus of this paper, such as the aging population for investigation of neurodegenerative disease diagnosis and progression monitoring.

As the PDs and the LEDs of the device are sealed with PDMS, the presence of biofluids, such as sweat, have negligible effects on the electrical performance of the device. In addition, given the high transparency of sweat in the NIR region of the spectrum—being largely composed of water with trace dopants—the introduction of sweat alone will not decrease the DC amplitude or AC signals of the patient. However, the introduction of artifacts due to sweat at the optical coupling interface (such as delamination) may influence the measurement. Although the data show no such effects during our clinical studies, the operation during high-sweat-rate events (such as physical exercise) requires further investigation.

Continuous monitoring of cerebral vascular tone provides insights into the transient states of cerebral autoregulation (49); high levels of cerebral autoregulation are associated with improved outcomes in patients with brain injury (46). The results presented here demonstrate wireless measurements of cerebral pulse pressure and vascular tone. The methods for measuring pulse pressure and cerebral vascular tone rely on strategies reported in the context of clinical studies across a wide-ranging age group, from premature neonates to older adults (2–4). Optical measurements of the pulse reflect changes in the diameter (and therefore volume) of arteries during the pulse cycle. These volumetric changes cause differences in the local concentration of hemoglobin over the volume explored by the measurements, and of the associated light absorption. The change in diameter of the arteries follows from variations in pulse pressure, closely related to vascular tone. As a consequence, although the absolute value of the optical pulse amplitude only loosely relates to pulse pressure, rapid variations in the amplitude of the optical pulse may be linked to variations in pulse pressure and vascular tone. Moreover, pulse pressure in the brain is difficult to measure directly—but sudden drops in this pressure may have significant clinical effects. Measurement of pulse amplitude can provide useful information about states of cerebral vasodilation (2). A number of additional factors, however, can influence pulse amplitude such as changes in the optical-coupling interface due to sweat or motion artifacts. Under controlled laboratory settings, results reported here support the validity of using pulse amplitude to determine cerebral vascular tone. Future studies will explore the applicability of this method during physical activities and in various clinical scenarios. This platform features simultaneous measurements of both systemic and cerebral hemodynamic monitoring through the differentiation of source–detector distances. Systematic tests indicate feasibility for recording cerebral oxygenation and cerebral vascular tone through optical measurements of pulse pressure during a breath hold at end inspiration with young adult subjects (Fig. 4). Further studies demonstrate capabilities in both systemic hemodynamics (HR and SpO_2) through use of signals captured at multiple source–detector distances and their corresponding tissue depths. This system may provide further insights into the interactions between systemic and cerebral hemodynamics, crucial for cerebral autoregulation monitoring, especially for patients susceptible to impaired cerebral flow, such as premature neonates (50) and hemodynamically unstable pediatric intensive care unit patients.

Pilot studies on pediatric CCHS patients highlight the effectiveness in continuous monitoring of pediatric patients with

disorders of autonomic regulation. The results indicate high accuracy and precision during continuous, wireless monitoring of cerebral oxygenation in four clinical physiologic challenges: HUT, hyperoxia, hypoxia, and hypoxia–hypercapnia as compared with data collected using clinical-standard monitoring instruments. Further, clinical studies may validate monitoring of cerebral hemodynamic parameters beyond those reported here, such as cerebral blood flow, cerebral pulse pressure, and cerebral hemoglobin concentrations.

The engineering approaches reported here strongly leverage nursing input for robust and clinically focused designs, featuring flexible mechanics for gentle, conforming interfaces and effective optical coupling to highly curved body parts and miniaturized sizes for pediatric subjects. The replaceable battery approach and the continuous, wireless, and real-time monitoring of cerebral hemodynamics suggest the potential for clinical use and broad scalability. Pilot clinical studies indicate feasibility for use on a variety of age groups (from infants to young adults), skin colors, and sex. The outcomes have the potential to enhance neonatal and pediatric care in clinical environments, including but not limited to peri- and postoperative recovery, cerebral hemodynamics monitoring on infants in anticipation of potential cerebral lesions induced by the immaturity of their neurovascular autoregulation system, and continuous monitoring of patients with inherent impaired autoregulatory systems. Further clinical validation may broaden the application of this system to both enhance global health in low-resource environments, as well as advancing current state-of-the-art clinical practices for prevention and investigation of cerebral pathologies.

Materials and Methods

Device Fabrication. Fabrication began with a 25-μm-thick polyimide sheet, with 12-μm-thick Cu on both sides (AP7164R; Dupont) and outlined using an ultraviolet laser cutter (ProtoLaser U4; LPKF). Electronic and sensor components, along with a pair of magnets (5862K13; McMaster Carr), were bonded to the circuit board by solder paste (TS391LT; Chip Quik). The board was folded and encapsulated within thin layers of medical-grade silicone (Silbione RTV 4420; Elkem) defined by an aluminum mold and subsequently filled with soft silicone (Ecoflex 00-10; Smooth-On). The final shape was outlined using a CO_2 laser cutter (VLS3.5; Universal Laser).

Data Analytics. All analyses used MATLAB (R2019b) for technical computing. A moving mean window of 5 s was applied to all analyses. The following hemodynamic parameters were used during the analysis (51): $\varepsilon_{Hb,740nm} = 0.40$, $\varepsilon_{Hb,850nm} = 0.19$, $\varepsilon_{HbO_2,740nm} = 0.13$, $\varepsilon_{HbO_2,850nm} = 0.25$, $DPF_{R-IR} = 1.3$, and h ranged between 5.5×10^{-4} and 6.2×10^{-4} (nm^{-1}) for 850 nm and between 6.3×10^{-4} and 7.2×10^{-4} (nm^{-1}) for 740 nm, empirically determined.

Clinical Studies. Clinical studies were performed under the permission of the Institutional Review Board (IRB no. 2017-1376) at Ann & Robert H. Lurie Children's Hospital of Chicago. Patients were recruited from clinical practice at the Center for Autonomic Medicine in Pediatrics in the division of Autonomic Medicine at Ann & Robert H. Lurie Children's Hospital of Chicago. A consent was read to each family prior to the study. After the staff answered all questions raised by the family, consent was then signed by families and the staff obtaining consent. Copies of the signed consents were given to each family and sent to health information management to be placed in a patient's medical record. Detailed protocols of clinical studies appear in *SI Appendix*.

Statistical Analysis. Cerebral oxygenation during tilt and recovery periods was compared with the initial baseline period. Statistical analysis was performed via paired Student t tests. $P < 0.05$ was considered statistically significant.

Data Availability. All study data are included in the paper and *SI Appendix*.

ACKNOWLEDGMENTS. A.Y.R. gratefully acknowledges funding support by the NIH's National Center for Advancing Translational Sciences, grant TL1TR001423. D.E.W.-M. and J.A.R. acknowledge funding from the Bill & Melinda Gates Foundation (OPP1182909). J.A.R. acknowledges additional funding from the Bill & Melinda Gates Foundation (OPP1193311). D.E.W.-M. and J.A.R. acknowledge support from the Gerber Foundation. J.A.R. also recognizes support from Save the Children (award 999002170). Z.X. acknowledges support from the National Natural Science Foundation of China (Grant 12072057) and Fundamental Research Funds for the Central Universities [Grant DUT20RC(3)032]. Y.H. acknowledges support from NSF (CMMI1635443). E.S. recognizes funding support from the Weinberg College of Arts and Sciences Undergraduate Research Grant Program, which is administered by Northwestern University's Weinberg College of Arts and Sciences. The conclusions, opinions and other statements in this publication are the authors' and not necessarily those of the sponsoring institution. This work is also supported by the National Natural Science Foundation of China (11402134 and 11320101001), the National Basic Research program of China (2015CB351900), and the NSF (1400159, 1534120 and 1635443). The materials and engineering efforts were supported by the Querrey Simpson Institute for Bioelectronics at Northwestern University. This work utilized Northwestern University Micro/Nano Fabrication Facility, which is partially supported by Soft and Hybrid Nanotechnology Experimental Resource (NSF ECCS-1542205), the Materials Research Science and Engineering Center (DMR-1720139), the State of Illinois, and Northwestern University. This work made use of the Central Laboratory for Materials Mechanical Properties with support from the Materials Research Science and Engineering Centers program of the NSF (DMR-1720139) at the Northwestern University Materials Research Science and Engineering Center.

1. M. S. Carroll *et al*., Residual chemosensitivity to ventilatory challenges in genotyped congenital central hypoventilation syndrome. *J Appl Physiol (1985)* **116**, 439–450 (2014).
2. Z. A. Vesoulis, A. M. Mathur, Cerebral autoregulation, brain injury, and the transitioning premature infant. *Front Pediatr.* **5**, 64 (2017).
3. K. L. Zaleski, B. D. Kussman, Near-infrared spectroscopy in pediatric congenital heart disease. *J. Cardiothorac. Vasc. Anesth.* **34**, 489–500 (2020).
4. Y. Yu *et al*., Cerebral near-infrared spectroscopy (NIRS) for perioperative monitoring of brain oxygenation in children and adults. *Cochrane Database Syst. Rev.* **1**, CD010947 (2018).
5. S. B. S. Serena *et al*., Young age as a risk factor for impaired cerebral autoregulation after moderate to severe pediatric traumatic brain injury. *Anesthesiology J. Am. Soc. Anesthesiologists* **108**, 588–595 (2008).
6. Y. Udomphorn, W. M. Armstead, M. S. Vavilala, Cerebral blood flow and autoregulation after pediatric traumatic brain injury. *Pediatr. Neurol.* **38**, 225–234 (2008).
7. T. Alderliesten *et al*., Low cerebral oxygenation in preterm infants is associated with adverse neurodevelopmental outcome. *J. Pediatr.* **207**, 109–116.e2 (2019).
8. C. J. Rhee *et al*., Neonatal cerebrovascular autoregulation. *Pediatr. Res.* **84**, 602–610 (2018).
9. S. H. Faridi, V. K. Srivastava, M. F. Hoda, M. Khalid, Accidental penetrating brain injury through anterior fontanelle: A rare phenomenon. *J. Forensic Leg. Med.* **19**, 109–110 (2012).
10. F. van Bel, J. Vaes, F. Groenendaal, Prevention, reduction and repair of brain injury of the preterm infant. *Front. Physiol.* **10**, 181 (2019).
11. P. Shah, S. Riphagen, J. Beyene, M. Perlman, Multiorgan dysfunction in infants with post-asphyxial hypoxic-ischaemic encephalopathy. *Arch. Dis. Child. Fetal Neonatal Ed.* **89**, F152–F155 (2004).
12. K. J. Goitein, I. Tamir, Cerebral perfusion pressure in central nervous system infections of infancy and childhood. *J. Pediatr.* **103**, 40–43 (1983).
13. D. E. Weese-Mayer, C. M. Rand, A. Zhou, M. S. Carroll, C. E. Hunt, Congenital central hypoventilation syndrome: A bedside-to-bench success story for advancing early diagnosis and treatment and improved survival and quality of life. *Pediatr. Res.* **81**, 192–201 (2017).
14. F. van Bel, J. P. Mintzer, Monitoring cerebral oxygenation of the immature brain: A neuroprotective strategy? *Pediatr. Res.* **84**, 159–164 (2018).
15. S. Chakravarti, S. Srivastava, A. J. Mittnacht, Near infrared spectroscopy (NIRS) in children. *Semin. Cardiothorac. Vasc. Anesth.* **12**, 70–79 (2008).
16. E. H. Austin, 3rd *et al*., Benefit of neurophysiologic monitoring for pediatric cardiac surgery. *J. Thorac. Cardiovasc. Surg.* **114**, 707–715, 717, discussion 715–716 (1997).
17. K. Meyer-Wiethe, F. Sallustio, R. Kern, Diagnosis of intracerebral hemorrhage with transcranial ultrasound. *Cerebrovasc. Dis.* **27** (suppl. 2), 40–47 (2009).
18. E. R. Muir *et al*., Quantitative cerebral blood flow measurements using MRI. *Methods Mol. Biol.* **1135**, 205–211 (2014).
19. Y. H. Kim *et al*., Cerebral perfusion monitoring using near-infrared spectroscopy during head-up tilt table test in patients with orthostatic intolerance. *Front. Hum. Neurosci.* **13**, 55 (2019).
20. P. Yao, W. Guo, X. Sheng, D. Zhang, X. Zhu, "A portable multi-channel wireless NIRS device for muscle activity real-time monitoring" in *2014 36th Annual International Conference of the IEEE Engineering in Medicine and Biology Society* (IEEE, 2014), pp. 3719–3722.
21. J. Jeppesen, S. Beniczky, P. Johansen, P. Sidenius, A. Fuglsang-Frederiksen, Exploring the capability of wireless near infrared spectroscopy as a portable seizure detection device for epilepsy patients. *Seizure* **26**, 43–48 (2015).
22. M. Broom, A. M. Dunk, A. L. E Mohamed, Predicting neonatal skin injury: The first step to reducing skin injuries in neonates. *Health Serv. Insights* **12**, 1178632919845630 (2019).

23. H. U. Chung *et al*., Skin-interfaced biosensors for advanced wireless physiological monitoring in neonatal and pediatric intensive-care units. *Nat. Med.* **26**, 418–429 (2020).
24. I. E. Olsen, S. A. Groveman, M. L. Lawson, R. H. Clark, B. S. Zemel, New intrauterine growth curves based on United States data. *Pediatrics* **125**, e214–e224 (2010).
25. P. Pinti *et al*., The present and future use of functional near-infrared spectroscopy (fNIRS) for cognitive neuroscience. *Ann. N. Y. Acad. Sci.* **1464**, 5–29 (2020).
26. P. Zaramella *et al*., Brain auditory activation measured by near-infrared spectroscopy (NIRS) in neonates. *Pediatr. Res.* **49**, 213–219 (2001). Erratum in: *Pediatr. Res.* **72**, 655 (2012).
27. D. J. W. William, A. Rutala; H. I. C. P. A. Committee, "Guideline for disinfection and sterilization in healthcare facilities" (Centers for Disease Control and Prevention, 2008).
28. S. Yan, A. P. Tran, Q. Fang, Dual-grid mesh-based Monte Carlo algorithm for efficient photon transport simulations in complex three-dimensional media. *J. Biomed. Opt.* **24**, 1–4 (2019).
29. A. P. Tran, S. Yan, Q. Fang, Improving model-based functional near-infrared spectroscopy analysis using mesh-based anatomical and light-transport models. *Neurophotonics* **7**, 015008 (2020).
30. I. S. Gousias *et al*., Magnetic resonance imaging of the newborn brain: Manual segmentation of labelled atlases in term-born and preterm infants. *Neuroimage* **62**, 1499–1509 (2012).
31. M. Jermyn *et al*., Fast segmentation and high-quality three-dimensional volume mesh creation from medical images for diffuse optical tomography. *J. Biomed. Opt.* **18**, 86007 (2013).
32. H. Dehghani *et al*., Near infrared optical tomography using NIRFAST: Algorithm for numerical model and image reconstruction. *Commun. Numer. Methods Eng.* **25**, 711–732 (2008).
33. A. Y. Rwei, W. Wang, D. S. Kohane, Photoresponsive nanoparticles for drug delivery. *Nano Today* **10**, 451–467 (2015).
34. M. Lindkvist, G. Granåsen, C. Grönlund, Coherent derivation of equations for differential spectroscopy and spatially resolved spectroscopy: An undergraduate tutorial. *Spectrosc. Lett.* **46**, 243–249 (2013).
35. N. L. Ekaterina, V. T. Valery, V. M. Igor, Measurements of absorbance of hemoglobin solutions incubated with glucose. *Proc. SPIE* **6791**, 67910O (2008).
36. C. Limperopoulos *et al*., Cerebral hemodynamic changes during intensive care of preterm infants. *Pediatrics* **122**, e1006–e1013 (2008).
37. T. W. L. Scheeren, P. Schober, L. A. Schwarte, Monitoring tissue oxygenation by near infrared spectroscopy (NIRS): Background and current applications. *J. Clin. Monit. Comput.* **26**, 279–287 (2012).
38. J. A. Filosa, Vascular tone and neurovascular coupling: Considerations toward an improved in vitro model. *Front. Neuroenergetics* **2**, 16 (2010).
39. J. D. Tobias, Cerebral oxygenation monitoring: Near-infrared spectroscopy. *Expert Rev. Med. Devices* **3**, 235–243 (2006).
40. V. B. Sivarajan, D. Bohn, Monitoring of standard hemodynamic parameters: Heart rate, systemic blood pressure, atrial pressure, pulse oximetry, and end-tidal CO2. *Pediatr. Crit. Care Med.* **12** (suppl. 4), S2–S11 (2011).
41. J. Li *et al*., The influence of systemic hemodynamics and oxygen transport on cerebral oxygen saturation in neonates after the Norwood procedure. *J. Thorac. Cardiovasc. Surg.* **135**, 83–90, 90.e1–90.e2 (2008).
42. T. Y. Abay, P. A. Kyriacou, Photoplethysmography for blood volumes and oxygenation changes during intermittent vascular occlusions. *J. Clin. Monit. Comput.* **32**, 447–455 (2018).
43. J. Kim *et al*., Miniaturized battery-free wireless systems for wearable pulse oximetry. *Adv. Funct. Mater.* **27**, 1604373 (2017).
44. M. Fabiani *et al*., Taking the pulse of aging: Mapping pulse pressure and elasticity in cerebral arteries with optical methods. *Psychophysiology* **51**, 1072–1088 (2014).
45. A. M. Chiarelli *et al*., Assessment of cerebrovascular development and intraventricular hemorrhages in preterm infants with optical measures of the brain arterial pulse wave. *J. Cereb. Blood Flow Metab.* **39**, 466–480 (2019).
46. L. A. Steiner *et al*., Continuous monitoring of cerebrovascular pressure reactivity allows determination of optimal cerebral perfusion pressure in patients with traumatic brain injury. *Crit. Care Med.* **30**, 733–738 (2002).
47. U. Salma, M. J. Ferdous, M. R. Alam, T. Barua, E. Jahan, "LED's optimum duty cycle in heart rate and oxygen saturation level combinedly measurement device for low power consumption" in *8th International Conference on Electrical and Computer Engineering* (IEEE, 2014), pp 13–16.
48. M. Thavasothy, M. Broadhead, C. Elwell, M. Peters, M. Smith, A comparison of cerebral oxygenation as measured by the NIRO 300 and the INVOS 5100 Near-Infrared Spectrophotometers. *Anaesthesia* **57**, 999–1006 (2002).
49. M. Czosnyka, K. Brady, M. Reinhard, P. Smielewski, L. A. Steiner, Monitoring of cerebrovascular autoregulation: Facts, myths, and missing links. *Neurocrit. Care* **10**, 373–386 (2009).
50. S. Noori, T. A. Stavroudis, I. Seri, Systemic and cerebral hemodynamics during the transitional period after premature birth. *Clin. Perinatol.* **36**, 723–736, (2009).
51. W. G. Zijlstra, A. Buursma, W. P. Meeuwsen-van der Roest, Absorption spectra of human fetal and adult oxyhemoglobin, de-oxyhemoglobin, carboxyhemoglobin, and methemoglobin. *Clin. Chem.* **37**, 1633–1638 (1991).